



Designing high-efficiency cryogenic regenerators: The role of microstructure and geometry in magnetocaloric cooling

Dmitriy Yu. Karpenkov^{a,b,*}, Rodion A. Makarin^b, Christian Tantardini^c, Alexander G. Kvashnin^d, Alexey Yu. Karpenkov^a, Efim V. Argunov^a, Tatyana A. Sviridova^a, Tatyana B. Shapaeva^b, Mark V. Zheleznyi^{a,e,f}

^a NUST MISIS, Leninskiy pr., 4, Moscow, Russia

^b Lomonosov MS, Leninskie Gory, 1, Moscow, Russia

^c Center for Integrative Petroleum Research, King Fahd University of Petroleum and Minerals, Dhahran 31261, Saudi Arabia

^d Skolkovo Institute of Science and Technology, Skolkovo Innovation Center, Bolshoy boulevard 30, Moscow 121205, Russia

^e Baikov Institute of Metallurgy and Materials Science, Leninskiy pr., 49, Moscow, Russia

^f MIREA – Russian Technological University, Moscow 119454, Russia



ARTICLE INFO

Keywords:

Magnetocaloric effect
RCO₂ family compounds
Heat-exchangers simulation
DFT calculation
Quenched-in vacancies
Defect-controlled DOS engineering

ABSTRACT

Rare-earth intermetallic RCo₂ compounds (R = Dy, Er, Ho, Tb, Gd) are among the most efficient solid-state refrigerants for hydrogen- and helium-temperature cryocoolers, yet their practical deployment is limited by thermal hysteresis that accompanies the first-order magnetic phase transition typical of heavy-R compounds. Here, we show that rapid melt-spinning—which freezes a high density of quenched-in Er-sublattice vacancies—provides a microstructural lever to transform the first-order phase transition (FOPT) in ErCo₂ and HoCo₂ into a continuous, second-order phase transition (SOPT) without rare-earth substitution. Magnetization, heat-capacity and magnetocaloric measurements on 30–150 μm ribbons reveal (i) a Curie-temperature rise of ~20 K, (ii) spontaneous-magnetization enhancement, and (iii) a three- to four-fold reduction of the isothermal entropy change, ΔS_T, in the as-spun state. First-principles calculations attribute these effects to vacancy-induced fulfilling of the Stoner criterion $JN(\epsilon_F) > 1$ at weaker exchange fields, and stabilizes band ferromagnetism with SOPT character. Post-quench annealing heals the vacancies, reinstating the FOPT and the large ΔS_T, confirming the causal role of defect-controlled DOS engineering. Compounds that are intrinsically second-order (R = Tb, Gd) remain largely insensitive to rapid quenching, underscoring the transition-order specificity of the mechanism. Coupled computational fluid-dynamics/heat-transfer simulations of regenerative cryocoolers demonstrate that 30 μm-thick, rapidly-quenched RCo₂ plates integrated into plate-fin regenerators deliver superior cooling power—compared with packed-bed geometries—under gaseous-helium flow, owing to lower porosity and shortened thermal diffusion lengths that permit higher operating frequencies. The synergy between vacancy-engineered magnetism and thin-plate morphology positions rapid quenching as a scalable route to structurally robust, thermodynamically optimized magnetocaloric exchangers for next-generation cryogenic refrigeration and energy-conversion technologies.

1. Introduction

Magnetocaloric materials (MCMs) have gained significant attention as a promising solid-state cooling medium, offering a solid-state, energy-efficient alternative to traditional gas-compression systems [1–3]. Among these materials, rare-earth-based intermetallic RCo₂ family compounds, where R is a rare-earth element, are notable for their

exceptional performance at cryogenic temperatures [4,5]. These compounds with R=Dy, Er and Ho undergo first-order magnetic phase transitions near their ordering temperatures, leading to significant magnetic entropy changes that can be finely tuned through rare-earth substitution [6].

The strong interaction between 3d (Co) and 4f (R) electrons in RCo₂ allows for precise control over transition temperatures and entropy

* Corresponding author at: NUST MISIS, Leninskiy pr., 4, Moscow, Russia.

E-mail address: [karpenkov.dy@misis.ru](mailto:karpennkov.dy@misis.ru) (D.Yu. Karpenkov).

changes, as highlighted in [7,8]. Because first-order phase transitions (FOPT) suffer from thermal hysteresis, it is advantageous to tune the material toward the critical point—the unique pressure-temperature-composition condition where FOPT behavior continuously transforms into second-order phase transition (SOPT) behavior. At this point latent heat and hysteresis disappear while the magnetocaloric effect remains large, giving the best balance between cooling power and reversibility [9,10]. Achieving this balance is crucial for optimizing both static thermodynamic efficiency and dynamic cyclic stability, which are key challenges for practical applications in magnetic refrigeration and energy conversion technologies [11]. The physical properties of RCO_2 intermetallic compounds are highly sensitive to external perturbations, including external pressure [12,13], microstructure engineering [14–16], and chemical substitution [17–22].

These phenomena are fundamentally linked to the inherent instability of the metamagnetic Co sublattice, which operates near critical conditions for moment formation. The Fermi level of the d -band in RCO_2 compounds lies on the descending part of the density of states (DOS) energy dependence, leading to unique magnetic behaviors, including itinerant metamagnetism of the cobalt subsystem [23]. Studies have shown that disorder in the Co sublattice narrows the $3d$ DOS, significantly enhancing the DOS at the Fermi energy and altering magnetic properties [24]. Additionally, a proposed mechanism explains how reducing the density of d -electrons shifts the Fermi level to lower energies within the rigid-band model, increasing the DOS at the Fermi level [25]. This shift ensures that the d -electron system satisfies the Stoner criterion for band ferromagnetism ($JN(\varepsilon_F) > 1$), where J is the Stoner exchange integral and $N(\varepsilon_F)$ is the density of states at the Fermi level. As a result, cobalt becomes magnetized under weaker effective exchange fields from the rare-earth (R) subsystem, which leads to an increase in the Curie temperature (T_C). Consequently, the phase transition order can be adjusted by calibrating the DOS at the Fermi level.

For practical applications, it is crucial to adapt magnetocaloric materials for implementation in heat exchangers. Designing these materials for cryogenic temperatures involves addressing challenges related to material homogeneity, structural integrity, and heat exchange efficiency. To maximize heat transfer, they are engineered with large surface areas and optimized flow paths for working fluids such as liquid nitrogen and helium. Common heat exchanger designs include plate-fin, shell-and-tube, and spiral configurations. Among the various fabrication techniques, rapid melt quenching via melt spinning has emerged as a highly effective approach for producing magnetocaloric materials in the form of ribbons with thicknesses ranging from 30 to 150 μm [26], allowing effective incorporation into magnetocaloric heat exchange devices.

In the present study, the influence of rapid quenching on the magnetism of the Co sublattice in RCO_2 compounds is comprehensively examined. Particular attention is given to the impact of this process on the magnetothermal properties of the Co_2 subsystem, with emphasis on the role of quenched-in vacancies and their reversible formation and elimination.

2. Experimental details

The specimens of ErCo_2 , HoCo_2 , TbCo_2 , and GdCo_2 were synthesized in an argon atmosphere using an induction furnace. The purity of the cobalt (Co) and rare-earth metals used was 99.99 % and 99.9 %, respectively. From the initial ingot, 10 g pieces were melt-spun into ribbons at wheel speeds ranging from 20 to 40 m/s using a Melt Spinner SC (Edmund Bühlér, Germany). The elemental and phase composition of the samples was verified through scanning electron microscopy (SEM) with a Tescan Vega 3 microscope and X-ray phase analysis using a DRON-4 diffractometer. The crystal lattice parameters were determined using Rietveld refinement. Temperature-dependent magnetization measurements were conducted using a PPMS 9 system (Quantum Design, USA). The magnetocaloric effect was measured in magnetic

fields of up to 1.8 T using the direct method, with a copper-constantan thermocouple for temperature detection. A detailed description of the experimental setup, including its calibration, is provided in the Supplementary materials of [27].

For Belov–Arrott (BA) analysis, demagnetizing-field corrections were applied to all isotherms. We considered only isotherms exhibiting minor hysteresis (< 1 % loop area) to ensure reversibility. The local field exponent $n(T) = \partial \ln |\Delta S| / \partial \ln H$ was computed from reversible ΔS_T data. Classification of the order of phase transition required (i) an S-shaped BA curve just above T_C ; (ii) $n > 2$ within $|T - T_C| \lesssim 2$ K for first-order behavior; absence of these features, together with $n \approx 2$ at T_C , indicates a second-order transition.

Vacancy concentration in the specimen was evaluated by means of three techniques: i) we refined both Er-site and Co-site occupancy in Rietveld fits (including a micro-absorption correction and fixed scale factor). The statistical significance of adding the occupancy parameter was tested using the Hamilton R-ratio test at the 95 % confidence level; ii) additionally, the density of both cast and rapidly quenched samples was measured using a pycnometer (ULTRAPYC 1200e, Quantachrome, USA); iii) differential scanning calorimetry (DSC) using a Setaram setsys evolution calorimeter at a heating rate of 20 K/min under Ar atmosphere.

3. Computational details

The $Fd\bar{3}m$ primitive cell of ErCo_2 was optimized using a $20 \times 20 \times 20$ k -point grid centered at the Γ -point, employing a plane-wave basis set through the DFT+U [28] approach with the PBE DFT functional [29]. The values of U and J_0 were determined by comparing the experimental lattice constant ($a = 5.0495$ Å) with that calculated using ab-initio methods. Specifically, U was set to 1.0 eV and J_0 to 0.1 eV for the valence d -electrons of Er and Co, resulting in a lattice constant differing by 0.4 % compared to experimental value. We utilized optimized norm-conserving Vanderbilt pseudopotentials [30,31], wherein the $4f$ -electrons of Er were treated as core states due to the lanthanide contraction [32], which proved to be a suitable approximation.

The optimization process employed the BFGS algorithm [33–36], with convergence criteria set at interatomic forces less than 10^{-5} Ry/atom and a SCF energy threshold of 10^{-6} Ry. A Gaussian smearing function with a smearing value of 0.010 Ry was applied.

A $2 \times 2 \times 2$ supercell of ErCo_2 , containing 48 atoms, was generated from the optimized $Fd\bar{3}m$ primitive cell. Defective structures were constructed by removing one Co atom from each of two layers of the Co sublattice.

The atomic positions were re-optimized while keeping the Hubbard U and exchange parameter J_0 fixed, because no previous experimental data are available from which to refit these parameters. This approach provides a first-order model in which the small variations in Co and Er concentration are assumed not to alter U and J_0 . The resulting defective compositions are $\text{ErCo}_{1.94}$ for a single Co vacancy, $\text{ErCo}_{1.875}$ for two Co vacancies and $\text{Er}_{0.97}\text{Co}_2$ for a single Er vacancy.

The magnetic order of the three structures was determined by initializing an antiferromagnetic order for a collinear polarized SCF calculation, resulting in a final ferrimagnetic structure consistent with previous studies on ErCo_2 [7,37,38].

These calculations were performed using Quantum Espresso v7.2 [39,40].

Using obtained lattice parameters after relaxation the electronic states were determined using the Korringa–Kohn–Rostoker (KKR) Green's function method [41–43] employed in AKAI-KKR program [44–46], which relies on scattering theory rather than conventional wavefunction-based approaches. In this formalism, the electronic structure is obtained through the single-particle Green's function $G(r, r', E)$, which satisfies the Dyson equation. To address the partial site occupancy and substitutional disorder present in the ErCo_2 alloy, the

Coherent Potential Approximation (CPA) [47,48] was employed. The CPA replaces the disordered lattice by an effective medium characterized by an averaged t-matrix:

$$G_{LL'}^i = \sum_{L''} \tilde{G}_{LL'} \left[1 - (t_i - \tilde{t}) \tilde{G} \right]_{L''L}^{-1}$$

$\tilde{G}_{LL'}$ and \tilde{t} are Green's function and t-matrix respectively, It is known that CPA is an efficient approximation, and in this case:

$$\sum_{i=1}^n x_i G_{LL'}^i = \tilde{G}_{LL'}$$

This equation implies that the Green's function of the effective medium is obtained by computing a weighted average of the Green's functions corresponding to each component atom positioned at the origin within that medium. Exchange-correlation effects were treated within the Generalized Gradient Approximation (GGA) using the Perdew-Burke-Ernzerhof (PBE) functional and scalar-relativistic approximation (SRA). Here, the optimized coordinates of the crystal lattice ErCo_2 obtained in QE were used. The Spin polarization was explicitly accounted for to capture magnetic phenomena. Magnetic states were analyzed by performing calculations for both the Local Moment Disorder (LMD) and ferrimagnetic (FiM) configurations. The LMD model simulates magnetic disorder by averaging over the random orientations of local magnetic moments, effectively describing paramagnetic or disordered magnetic phases.

The exchange energy difference was evaluated as:

$$\Delta E_{\text{ex}} = E_{\text{LMD}} - E_{\text{FiM}}$$

where E_{LMD} and E_{FiM} are the total energies of the system in the local moment disorder and ferrimagnetic states, respectively.

Computational parameters during the self-consistent iterations included an imaginary energy component at the Fermi level of $\text{edel} = 0.001$ Ry to smooth the density of states, and an energy contour width of $\text{ewidth} = 1.2$ Ry for integration along the complex energy path. Angular momentum cutoffs for basis functions were set to $l_{\max} = 3$ for erbium and $l_{\max} = 2$ for cobalt, ensuring appropriate completeness of the basis set. At the final stage, densities of states (DOS) were computed utilizing an ultra-dense k -point mesh to achieve high-resolution electronic structure details necessary for subsequent analysis.

The magnetization of a material can be calculated from the spin-resolved integrated density of states (DOS) as follows:

$$M = \left| \int DOS(E)_\uparrow dE - \int DOS(E)_\downarrow dE \right| \times \mu_B \times \frac{N}{V},$$

Where V - unite cell volume, μ_B - Bohr magneton.

4. Heat transfer simulation

The maximum cooling power of the stacked plates and packed bed heat-exchangers based on RCO_2 family compounds was estimated using similarity theory in combination with an unsteady state heat transfer model. An extended description of the calculation routine can be found in [27].

The calculation was carried out under the assumption that the volume occupied by the magnetocaloric material has a cylindrical shape with a diameter of 40 mm and a length of 100 mm. The variable parameters that were examined included plate thickness (from 0.03 to 1 mm) and channel width (from 0.03 to 1 mm) for plate heat exchangers, as well as particle diameter (from 0.1 to 2 mm) for packed bed geometry.

The total pressure drops across the entire liquefier (including all heat exchangers, valves, and piping) is typically designed to remain well below 0.2 atm (0.02 MPa) to ensure efficient operation and avoid excessive compressor load. In contrast to conventional gas compression

cooling cycle, magnetic refrigerator operates on a fundamentally different principle, requiring the working fluid to be pumped through a refrigerant. Considering the mechanical stability and power consumption of the pump, the permissible pressure drop limit was set at 5 atm (0.5 MPa). Liquid and gaseous helium were utilized as the heat transfer medium (HTM), and modeling gasses phase was conducted at cryogenic temperatures, in proximity to the condensation point. ErCo_2 was selected as the material for the heat exchanger.

In order to simulate the process of heat transfer, the maximum velocity of the heat transfer fluid, V_{\max} , was estimated in the initial step. Considering all the limitations, the dependence of V_{\max} on channel width and particle size was calculated for a variety of heat exchangers. Numerical simulations revealed that, under an imposed pressure differential of 5 atm (0.5 MPa), plate-type heat exchangers consistently exhibited significantly higher flow velocities compared to packed bed systems irrespective of the phase state of the heat transfer medium. It is noteworthy that when gaseous helium is employed as a heat transfer medium, the pumping velocity exceeds those calculated for liquid heat transfer media by two orders of magnitude.

The cooling and heating processes subsequent to adiabatic magnetization and demagnetization cycles are regarded as unsteady thermal processes. Consequently, the predominant parameter that determines the heat transfer rate is thermal diffusivity α . It is noteworthy that the value of α varies for each case and must be calculated using the following equation: $\alpha = Nu \lambda_{\text{HTM}} / \delta$, where δ signifies the characteristic length of the structure (half of the plate width or particle diameter). The Nusselt numbers, Nu , for plate heat exchangers and ball-packed structures, are determined by (1–4).

In the case of liquid heat transfer fluid [49]:

$$Nu_{\text{stacked plates}} = 0.023 Re_{\text{HTM}}^{0.8} Pr_{\text{HTM}}^{0.3} (Pr_{\text{HEX}} / Pr_{\text{HTM}})^{0.25} \epsilon_l \epsilon_\delta \quad (1)$$

$$\epsilon_l = 1 + \frac{d}{L}, \quad \epsilon_\delta = \exp\left(0,85 \frac{s/\delta}{s/\delta_{\text{opt}}}\right) - \text{roughness correction}$$

$$Nu_{\text{packed bed}} = 0.4 Re_{\text{HTM}}^{0.5} Pr_{\text{HTM}}^{0.33} \quad (2)$$

In the case of gaseous heat transfer medium [50]:

$$Nu_{\text{stacked plates}} = 0.023 Re_{\text{HTM}}^{0.8} Pr_{\text{HTM}}^{0.4} \quad (3)$$

$$Nu_{\text{packed bed}} = 2 + 1,1 Re_{\text{HTM}}^{0.6} Pr_{\text{HTM}}^{0.33} \quad (4)$$

Importantly, achieving the device's maximum cooling power requires maximizing the mass of the heat exchanger. It should be emphasized that in order to achieve the highest possible cooling power of the device, the mass of the heat exchanger has to be maximized. Obviously, a higher porosity of the regenerator results in less material, thereby lower generated/absorbed heat Q_{gen} . The second important parameter influencing the cooling capacity is the efficiency of heat transfer between the solid refrigerant and the heat transfer medium. In an ideal scenario, the quantity of heat energy transferred to the heat transfer fluid during a single cycle would be equivalent to the generated heat Q_{gen} . The ratio of the actual transferred heat to Q_{gen} is defined as utilization factor k_u .

In the case of stacked plates heat exchangers, the optimum porosity corresponding $k_u = 1$ can be determined by optimizing the amount of heat transfer medium required for efficient heat transfer at different frequencies. The computational results indicate that the optimum porosity increases dramatically when the plate width decreases. This trend can be attributed to the fact that for 30 μm thick plates and porosity less than 10 % in the case of liquid helium and less than 37 % for gas, the channels are very narrow (less than 10 μm). Hence at our pressure drop limit of 5 atm it becomes impossible to circulate a sufficient volume of coolant through the regenerator to absorb all the generated heat Q_{gen} . Consequently, in order to maintain $k_u = 1$ it is necessary to increase the channel width—and thus the

porosity—although this simultaneously reduces the volume fraction of magnetocaloric material, leading to a decrease in the Q_{gen} . For comparison, the minimum porosity for packed bed of monodisperse spheres is 44 % irrespective of the particle size.

In the next step, the time dependences of the heat exchanger temperature as a result of forced cooling were calculated. The temperature of the heat transfer medium was kept constant at $T_{HTF} = 4$ K in the case of liquid medium and $T_{HTM} = 33$ K in the case of gas. At time zero, the temperature of the heat exchangers was set equal to $T_{HEX} = T_{HTM} + 3.5$ K. The latter value is equal to the maximum adiabatic temperature change obtained by changing the external magnetic field $\Delta\mu_0H = 2.0$ T [4,51]. After that, the heat exchanger is subjected to forced cooling through the pumping of a heat-transmitting liquid or gas. An analysis of the obtained data indicates that in the case of liquid helium, the heat flow in the packed bed heat exchanger is one order of magnitude higher than the heat transfer in the stacked plate heat exchanger, for the corresponding characteristic length of the structure (half-width of the plate or radius of the particle). This enhancement is primarily attributed to the increased surface area in the case of a porous body. However, when gaseous heat transfer media is employed, the scenario undergoes a substantial transformation. In case of packed bed heat exchangers, the relatively low velocity of gas helium circulated through the regenerator, rendering it insufficient to effectively remove all the generated heat in the magnetocaloric material. This results in packed bed heat exchangers being incapable of operating at frequencies above 1 Hz.

Using the obtained time dependences of the heat exchanger temperature under forced cooling, the CP cooling capacity provided by each type of heat exchanger were calculated.

Obviously, reducing the plate width or sphere diameter dramatically accelerates the heat transfer, thereby enabling the device to be operated at a higher frequency f , which in turn increases cooling power. At the same time, it leads to a decrease in the Q_{gen} of the stacked plate heat exchanger due to the reduction of the mass of the magnetocaloric material caused by the enhanced porosity of such a regenerator. A comprehensive evaluation was carried out to identify and quantify the key parameters affecting the performance of heat exchangers. We calculated the maximum cooling power CP_{max} for each geometry as a function of operating frequency and the results are shown in Fig. 1. For the optimal porosity ($k_u = 1$), the cooling power increases with frequency for all regenerators, but for the 30 μm thick plate CP_{max} reaches its maximum value, showing the optimal balance between the amount of material (which should be maximized) and the characteristic length of the structure (which should be minimized to accelerate heat transfer).

It should be noted that, owing to enhanced heat flux dynamics, the packed bed configuration exhibits a higher heat transfer rate compared to plate regenerators. However, when liquid helium is employed as the heat transfer medium 30 μm thick plates exceed the performance of the packed bed heat exchanger by ~50 %. This advantage is attributed to the lower porosity and consequently due to the higher amount of

magnetocaloric material. In the case of gaseous helium, a substantial enhancement in cooling capacity is observed, attributable to the accelerated pumping of the heat transfer fluid through the heat exchanger. This provides maximization of utilization factor.

Consequently, the utilization of plate heat exchangers with a thickness of 30 μm is proposed as a highly efficient solution for heat exchange in RCO_2 -based magnetic refrigerators. This proposal stands in contrast to the findings of other researchers [4,15], who applied the atomization technique for producing spherical particles for packed bed heat exchangers. For thin plates of approximately 30 μm thickness, a magnetic refrigerator operating at frequencies as low as 10 Hz can be created.

However, when producing such thin materials by conventional methods (electrical discharge cutting, grinding, etc.), one could encounter cracking problems, e.g. along grain boundaries during machining (the average size of polycrystalline grains is about a tenth of a micrometer and depends on the cooling rate after alloy melting). Reducing the grain size could improve mechanical stability, which could be achieved, for example, by rapidly quenching, giving the possibility of producing thin metal ribbons with good mechanical properties.

In this study, the melt spinning technique was employed to fabricate thin ribbons for RCO_2 ($R = Er, Ho, Tb, Gd$) compounds. The effect of rapid quenching on the magnetothermal properties of the obtained materials was also investigated.

Melt-spinning produces fine-grained ribbons (30–150 μm) that mitigate grain-boundary cracking relative to machined foils. The internal properties of magnetocaloric material is sufficient to withstand the bending and buckling deformation under explored pressure drop of 5 atm. Ribbons can be slit, stacked, and joined by diffusion bonding [25], low-heat-input laser spot welding, or mechanical clamping frames. The only factors that may compromise the mechanical integrity of the structure are: i) the fluid pressure could spread the entire stack, causing tension at the stack mounting; ii) hydrodynamic forces and vibrations may arise during fluid flow; and iii) thermal stresses (due to the low temperature of liquid helium). Functional fatigue from magnetostriction and flow-induced vibrations can be mitigated by the above geometrical reinforcements; helium is inert, and simple passivation or thin Cu/Ni over-plating suffices for handling or bonding without degrading magnetocaloric response.

5. Result and discussions

To investigate the influence of rapid quenching on the magnetocaloric properties, the key characteristics were measured, including the specific spontaneous magnetization (Fig. 2(a)), the isothermal entropy change (Fig. 2(b)), and the adiabatic temperature change (Fig. 2(c)).

The specific spontaneous magnetization is determined as the specific magnetization at the intersection between linear extrapolation of the high-field (paraprocess) region and the region of maximum magnetic permeability of the $M(H)$ curve back to zero field. In the $ErCo_2$ and

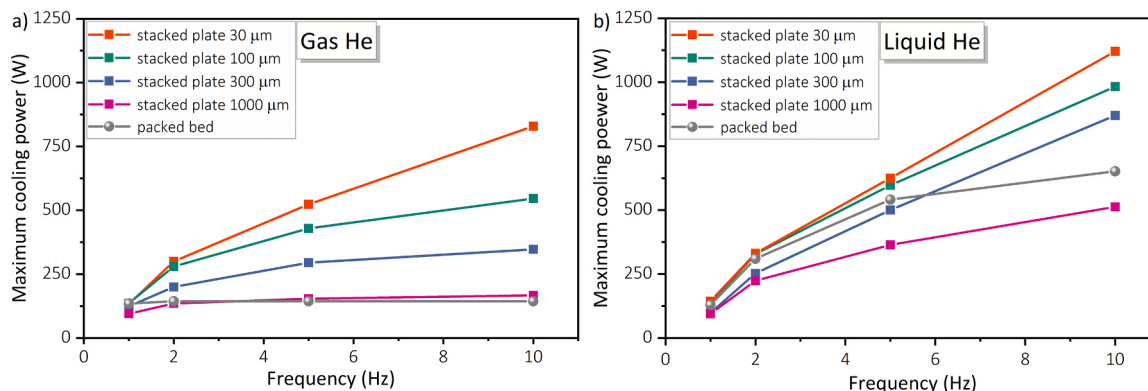


Fig. 1. Frequency dependence of cooling capacity for two heat exchanger geometries of $ErCo_2$.

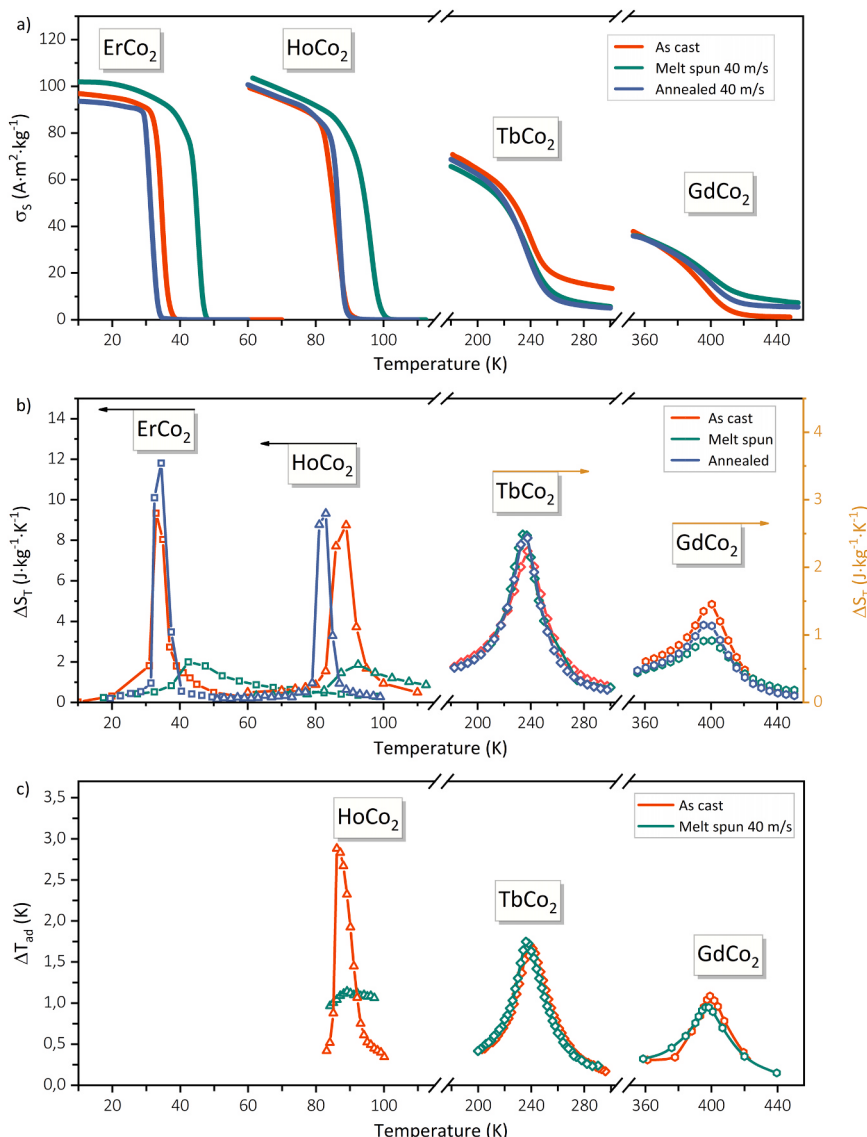


Fig. 2. Temperature dependences of (a) spontaneous specific magnetization, (b) isothermal entropy change in field of 2 T, (c) adiabatic temperature change in field of 1.85 T.

HoCo₂ alloys, rapid quenching caused the Curie temperature to shift to higher values ($\Delta T_C = 10$ K and $\Delta T_C = 8$ K, respectively) and increased the specific magnetization. After annealing, these parameters returned to values typical of the as-cast state, whereas the TbCo₂ and GdCo₂ alloys showed no similar changes.

A drastic suppression in the magnetocaloric effect was observed in the rapidly quenched samples of ErCo₂ and HoCo₂, possessing the first order of phase transition in as-cast state. In quenched ErCo₂, the maximum ΔS_T decreased from 9.75 to 2 J·kg⁻¹·K⁻¹ relative to the as-cast state. For HoCo₂ sample, the maximum ΔS_T decreased from 9.83 to 1.98 J·kg⁻¹·K⁻¹. Annealing fully recovered the magnetocaloric performance, achieving $\Delta S_T = 12$ J·kg⁻¹·K⁻¹ and $\Delta S_T = 10$ J·kg⁻¹·K⁻¹ for ErCo₂ and HoCo₂ respectively. Similarly, the adiabatic temperature change ΔT_{ad} in the quenched samples was approximately three times lower than in the cast state.

In contrast, the TbCo₂ and GdCo₂ alloys, which undergo a second-order phase transition, exhibited no significant variations in behavior. Rapid quenching had a minimal impact on their magnetocaloric response or Curie temperature.

The observed behavior in rapidly quenched ErCo₂ and HoCo₂ samples can be attributed to a shift in order of phase transitions [16]. To

verify this assumption, two analytical approaches were employed: the analysis of Belov-Arrott plots and the evaluation of isothermal entropy variations [9].

The temperature dependence of the exponent $n = d \ln|S_T|/d \ln H$, which describes the field dependence of the isothermal entropy change ($\Delta S \sim H^n$), is shown in Fig. 3. Second-order magnetic phase transitions are distinguished from first-order transitions by the critical value $n = 2$ (this level is indicated by the pink dividing line on plots). As shown in Fig. 3, the n values for the rapidly quenched samples (green data points) remain below or close to $n = 2$ across the entire temperature range, which indicates a second-order magnetic phase transition. In contrast, the as-cast (red) and annealed (blue) samples display a sharp increase in n near the Curie temperature, with values surpassing $n > 2$ - a hallmark of a first-order transition.

The insets of Fig. 3 present the Belov-Arrott plots $M^2(H/M)$. The annealed samples reveal a distinctive S-shaped curvature at temperatures slightly above T_C , indicating the presence of a first-order magnetic phase transition. In contrast, rapidly quenched samples exhibit an absence of this behavior and are characterized by linear or monotonic Belov-Arrott curves, thereby affirming their second-order nature.

The BA and n(T) criteria are fully consistent across the explored

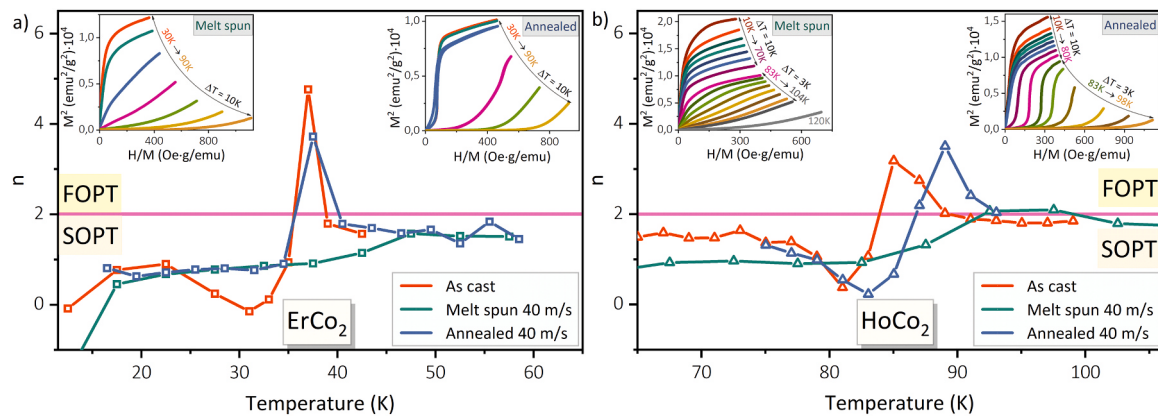


Fig. 3. Temperature dependence of the exponent n for as-cast, rapid quenched and annealed ErCo_2 and HoCo_2 samples. The value $n = 2$ marks the boundary of the phase transition of the first and second orders. In the inset, the graphs show the Belov-Arrott dependences for quenched and annealed samples.

range (Fig. 3). As-cast/annealed $\text{ErCo}_2/\text{HoCo}_2$ display an S-shape in M^2 vs H/M and $n > 2$ near T_C , whereas rapidly quenched samples show linear BA plots and $n \approx 2$ at T_C , indicative of second-order behavior.

A shift in the order of phase transition was previously reported in ErCo_2 samples produced via rapid quenching and atomization techniques [15,16]. While both treatments induce similar changes in material properties, the underlying mechanisms appear to differ. In atomized samples, the observed alteration in phase transition behavior and the shift of the Curie temperature have been attributed by the authors to variations in lattice parameters. However, this explanation contradicts results from studies on rapid quenching, where no significant changes in

lattice parameters were detected.

To elucidate this discrepancy, we conducted an analysis of X-ray diffraction data for cast, rapidly quenched, and annealed samples of all compounds investigated in this study (Fig. 4). As shown on right-hand yellow insets of the graphs in Fig. 4 our results confirm that the lattice parameters remain statistically invariant within experimental error across all processing conditions. This suggests that the lattice parameter variations reported in [15] likely stem from differences in phase composition rather than intrinsic structural changes. Supporting this hypothesis, we observed during sample preparation that even trace amounts (< 4 vol%) of an impurity phase with the stoichiometric

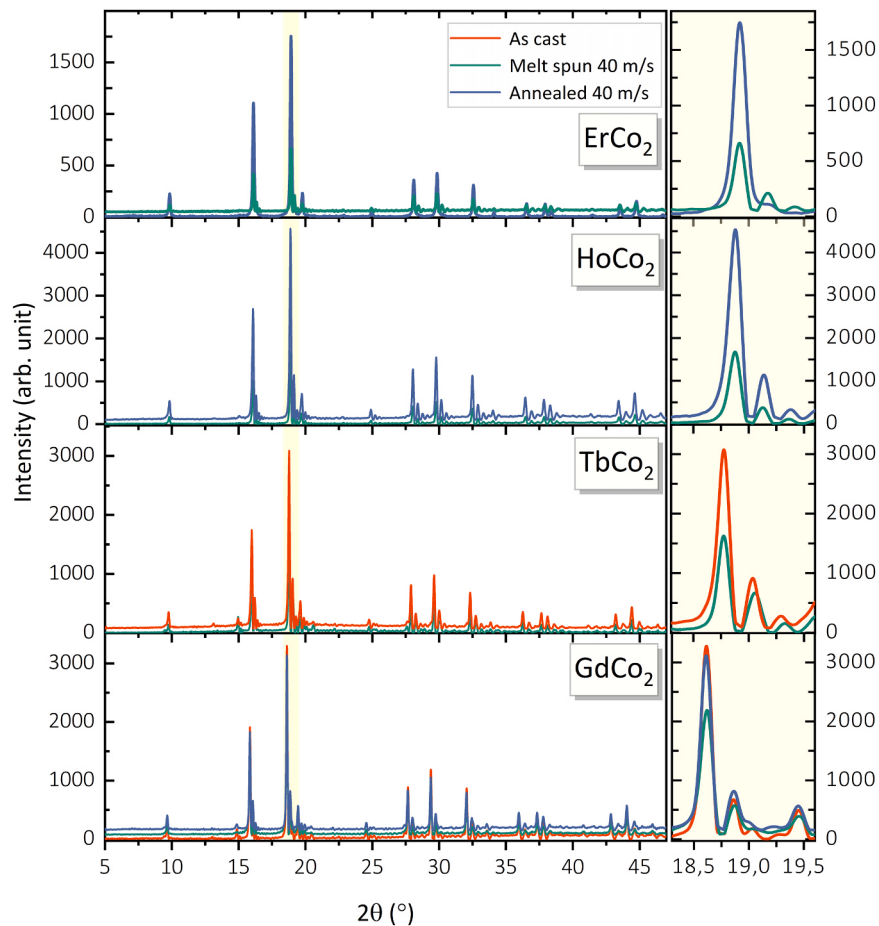


Fig. 4. XRD spectra for as-cast, rapidly quenched, and annealed samples of ErCo_2 , HoCo_2 , TbCo_2 , and GdCo_2 compounds.

composition of RCO_3 can significantly influence measured lattice parameters. Thus, we propose that the phase transition modifications in atomized samples [15] arise from secondary phase formation rather than lattice distortion—a distinction critical for interpreting property changes in these systems.

It is worth noting that the authors in [14,24] associate the change in properties with a variation in the electronic structure of the samples due to the formation of defects. Therefore, it is essential to investigate the change in the microstructure of rapidly quenched ribbons, since the latter inevitably affects the inherent instability of the metamagnetic Co sublattice. In turn, during the melt spinning process the occurrence of several types of defects is possible due to the presence of extreme thermal gradients and high cooling rates ($\sim 10^5\text{--}10^6 \text{ K/s}$). The main structural defects in melt-spun ribbons include a high density of dislocations and other crystallographic defects introduced by rapid solidification, internal stresses due to thermal gradients and constraint effects, and quenched-in vacancies or point defects [52–54]. These defects lead to inhomogeneous microstructures with spatial variations in phase composition and lattice distortions.

As demonstrated in [25], the presence of disorder in the cobalt sublattice results in a significant reduction of the $3d$ orbital density of states. This reduction has been shown to enhance the DOS at the Fermi energy, thereby resulting in a subsequent alteration of the magnetic properties. To model these changes via first-principles calculations—specifically, to track DOS evolution during quenching-induced vacancy formation—it is critical to take accurate measurements of the vacancy density.

During melt spinning of metals, the quenched-in vacancy concentration can reach up to 0.1–1 % of lattice sites. The actual value depends on cooling rate, sample size, and alloy composition. Three methods have been used in this work to determine vacancy concentration. The first method involves the measurement of sample density [55,56], the second method entails the analysis of X-ray spectra [57,58], and the third DSC method reveals the energy being stored in vacancies during rapidly quenching [59].

In this study, particular emphasis was placed on estimating the vacancy concentration in rapidly quenched ErCo_2 samples, as rapid quenching induces the most pronounced modifications in their magnetocaloric properties. Rietveld refinement of the diffractograms showed that the spectra were better described for ErCo_{2-x} composition within the Co content from 1.98 to 1.88, since the lowest reliability factors were

obtained (see Table 1). Additionally, the corresponding change in X-ray density during vacancy formation was estimated by varying the degree of atomic position occupancy. Direct density measurements using a pycnometer have shown that the density change $\Delta\rho = -90 \pm 30 \text{ kg/m}^3$ during rapid quenching. Converting $\Delta\rho$ to either Er or Co content using the propagating uncertainties yields $\text{ErCo}_{1.94\text{--}1.98}$ and $\text{Er}_{0.98\text{--}0.99}\text{Co}_2$ compositions.

Fig. 5 shows DSC thermograms taken at 20 K/min temperature ramping rate for ErCo_2 as-melt-spun ribbons. The pronounced exothermic effect is observed within the temperature range of 500–620 °C. The irreversibility of this event, evidenced by its absence upon subsequent cooling, suggests a structural relaxation process. This exothermic effect is therefore ascribed to the annihilation of lattice defects, specifically vacancies, that were in-quenched from the rapid solidification process. The total energy stored in these defects, calculated from the integrated area of the exothermic peak, is 6.95 J/g. Based on the assumption of a vacancy formation energy between 1 and 2 eV, we calculate a vacancy concentration of approximately 0.02 per formula unit. This value is consistent with a nominal compositional deviation, either $\text{Er}_{0.96}\text{Co}_2$ or $\text{ErCo}_{1.96}$.

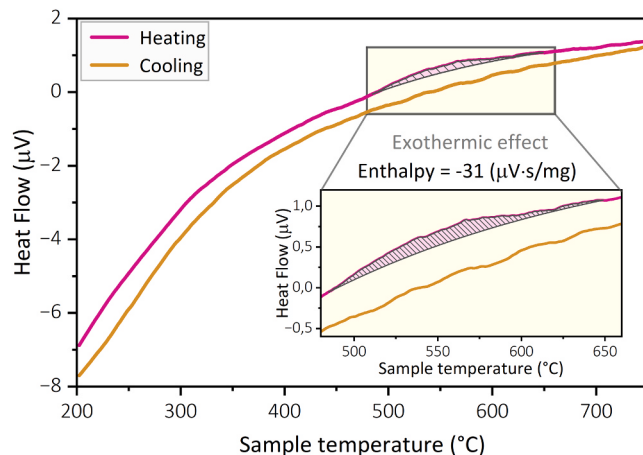


Fig. 5. DSC thermograms obtained for ErCo_2 rapidly quenched samples during heating and cooling protocols. The ramping rate was 20 K/min for all measurements.

Table 1
Reliability factors of ErCo_{2-x} compositions.

		Phase composition	R_{wp}	GOF	R_p
Er site vacancy	Er _{0.94} Co ₂	0.06	2.38	0.04	
	Er _{0.96} Co ₂	0.05	2.25	0.04	
	Er _{0.98} Co ₂	0.05	2.13	0.04	
	Er _{0.99} Co ₂	0.05	2.10	0.03	
nominal composition	ErCo ₂	0.06	2.04	0.03	
Co site vacancy	Er _{0.94} Co ₂	0.06	2.38	0.04	
	ErCo _{1.96}	0.05	2.00	0.03	
	ErCo _{1.94}	0.05	2.00	0.03	
	ErCo _{1.92}	0.05	2.00	0.03	
	ErCo _{1.90}	0.05	2.00	0.03	
	ErCo _{1.88}	0.05	1.99	0.03	
	ErCo _{1.86}	0.05	2.05	0.03	

Accordingly, the investigation of the quenching-in vacancies formation on the density of state for ErCo_2 compound were carried out for two compositions: $\text{ErCo}_{1.94}$ which closely approximates the experimentally observed vacancy concentration (corresponding to the removal of one Co atom per unit cell), and $\text{Er}_{0.97}\text{Co}_2$ representing a vacancy in Er site for comparative analysis.

The most important finding is related to pDOS of the d -orbitals that they are populated for energies below the energy Fermi without defects, see Fig. 6. This means that d -orbitals are responsible only for the magnetism of ferrimagnetic ErCo_2 .

We have calculated the change in the magnetization under introduction of vacancies at both Er and Co sites by subtracting the integrated of density of state for spin up and spin down zones. It was established that $\Delta M_{\text{Er,vac}} = 5\%$ in contrast to the $\Delta M_{\text{Co,vac}} = -5.5\%$. The removal of a Er atom stabilizes the magnetic ground state. The observed tendency agrees with the experimental observations, depicted in Fig. 2(a), and confirms that magnetic transitions in ErCo_2 can be driven by structural modifications. Indeed, the spin polarization has changed from a slightly ferrimagnetic structure to more intensity magnetic moment of Co with respect to Er that has also increased by the formation of Er-vacancies.

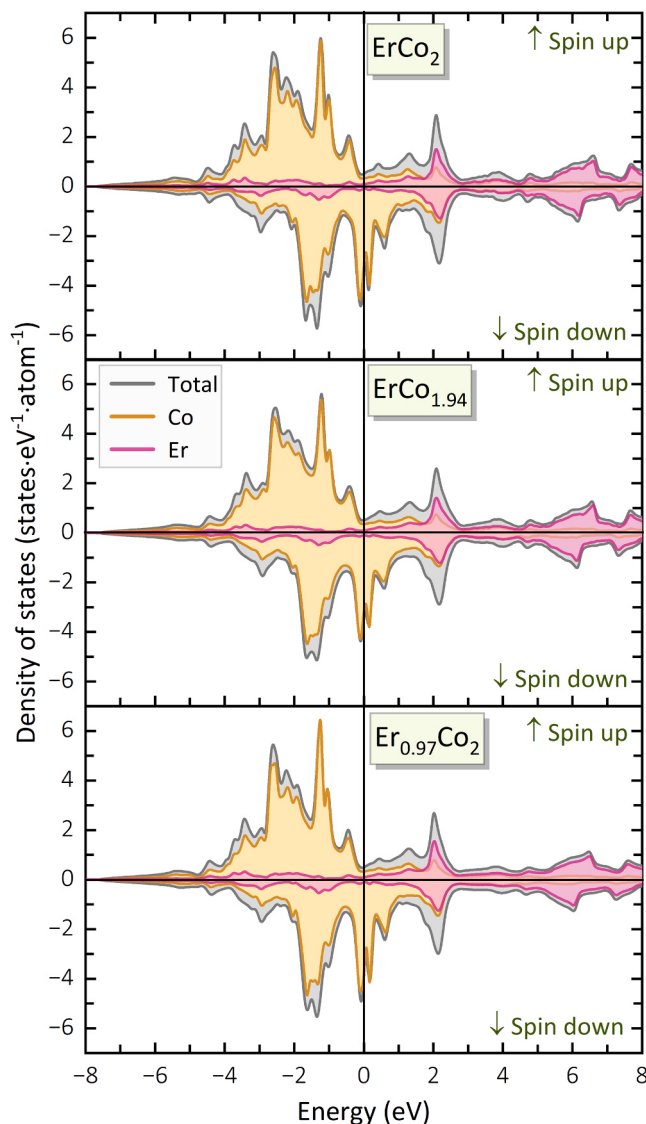


Fig. 6. Calculated electronic density of states (DOS) projected on the d -orbitals of Co and Er atoms rescaled by Fermi energy. Contribution from the d -bands of Er and Co atoms are shown by purple and brown colors. Majority spins are shown on the top and minority on the bottom panels of each figure.

Subsequently, for the three previously analyzed crystal structures we calculate the exchange energy as $\Delta E_{\text{ex}} = E_{\text{LMD}} - E_{\text{FIM}}$, where E_{LMD} and E_{FIM} are the total energies of the system in the local moment disorder and ferrimagnetic states, respectively. Using obtained data the following magnetic exchange integrals were evaluated: -0.18 eV for ErCo_2 , -0.164 eV for Co vacancy and -0.204 eV for Er vacancy. This data indicates that ErCo_2 prefer antiferromagnetic order over ferromagnetic order.

Introducing the Er site vacancy markedly enhances the stability of the antiferromagnetic order. However, as the number of Co vacancies increases, the antiferromagnetic order remains preferred, albeit with a slight decrease in stability compared to the previous structure.

Overall, our findings suggest a consistent preference for antiferromagnetic order in these crystal structures, even under different structural modifications, indicating the robustness of this magnetic arrangement in these systems.

To theoretically describe the modification of the magnetic behavior in the rapidly quenched samples in the case of ErCo_2 and HoCo_2 we employ the Stoner model of itinerant electrons. The model is applicable in the case of strong overlap of electronic levels (the width of the electronic levels exceed the distance between them) [60,61]. It is widely used to describe the behavior of metals, intermetallics and alloys with a d -electron subsystem. The following assumptions are adopted within this framework [62,63]: i) the magnetic electrons obey the Fermi-Dirac statistics and are independent; ii) for all RCO_2 intermetallic ($\text{R} = \text{Y}, \text{Lu}, \text{Sc}$ - paramagnetic in the exchange enhanced zone and $\text{R} = \text{Dy}, \text{Ho}, \text{Er}, \text{Tm}$ - multi-sublattice zone magnetism) the similarity of the $3d$ orbital structures is valid due to the similarity of the external electronic configurations of the rare earth (magnetic and non-magnetic); iii) the splitting of the subzones is small compared to their width; iv) the spin-spin interaction is present.

In this framework, the magnetization of the system is proportional to the difference in the population of the subzones $M = \mu_B(n_+ - n_-)$, where n_{\pm} is the number of electrons with up/down spins, which is given by the following equation

$$n_{\pm} = \int_0^{\zeta_{\pm}} N_{\pm}(\epsilon) f_{\pm}(\epsilon) d\epsilon \quad (5)$$

In these expressions, $N_{\pm}(\epsilon)$ is the density of electronic states with energy ϵ , ζ_{\pm} is the chemical potential. The total free energy is expressed as the sum of the kinetic energy of the itinerant electrons and the exchange energy of the spin-spin interaction. Given the small spin subzone splitting, the exchange energy can be expanded in a power series with respect to magnetization [62].

Ferromagnetism in the itinerant model is achieved under conditions of thermodynamic equilibrium $\partial F_d / \partial M_d = 0$ and $\partial F_d^2 / \partial^2 M_d \geq 0$, i.e., the Stoner criterion $JN(\epsilon_F) > 1$. In RCO_2 compounds, the Fermi level lies at the edge of the electronic $3d$ zone, as the result of the overlap of the $3d$ zone of Co and the $5d$ ($4d$) zone for rare earth elements [64]. In the theoretical description of multi-sublattice zone magnetics such as DyCo_2 , ErCo_2 , HoCo_2 , it is necessary to take into account the intrinsically effective molecular field acting on the part of the $4f$ electrons localized on the rare earth ions with momentum gJ .

This enhancement of the Stoner model is called the Inoue-Shimizu model or the s - d model [65–67]. In this model the free energy is written as $F = F_d + F_f - \lambda_{\text{Er-Co}} M_d M_f$, where F_d is the free energy of the above-mentioned subsystem of itinerant electrons, F_f is the free energy of the local moments, and $\lambda_{\text{Er-Co}}$ denotes the coefficient of the molecular field exerted on the itinerant electrons by the side of the local moments of the rare earth.

Thus, the free energy of the system can be expressed as power series expansion in even powers of magnetization:

$$F(M) = \frac{1}{2} A(T) M^2 + \frac{1}{4} B(T) M^4 + \frac{1}{6} C(T) M^6 - BM \quad (6)$$

The coefficient corresponding to the fourth-order magnetization term is calculated as follows [64]

$$B(T) = B_{itn}(T) + B_{loc}(T)$$

$$= B_{itn}(0)(1 + g_B T^2) + \frac{1}{720} N_{Er}(g_{Er}\mu_B\lambda_{Er-Co})^4 (kT)^{-3} [(2J_{Er} + 1)^4 - 1]$$

$$B_{itn}(0) = \frac{1}{6\mu_B^4 N^3(\varepsilon_F)} \left[3 \left(\frac{N'(\varepsilon_F)}{N(\varepsilon_F)} \right)^2 - \frac{N''(\varepsilon_F)}{N(\varepsilon_F)} \right]$$

$$g_B = \frac{(k\pi)^2}{6 \left[3 \left(\frac{N'(\varepsilon_F)}{N(\varepsilon_F)} \right)^2 - \left(\frac{N''(\varepsilon_F)}{N(\varepsilon_F)} \right) \right]} \left[15 \left(\frac{N'(\varepsilon_F)}{N(\varepsilon_F)} \right)^4 - 25 \frac{N^2(\varepsilon_F)N''(\varepsilon_F)}{N^3(\varepsilon_F)} \right. \\ \left. + 4 \left(\frac{N''(\varepsilon_F)}{N(\varepsilon_F)} \right)^2 + 7 \frac{N'(\varepsilon_F)N'''(\varepsilon_F)}{N(\varepsilon_F)^2} - \frac{N''''(\varepsilon_F)}{N(\varepsilon_F)} \right] \quad (7)$$

In (3) $N'(\varepsilon_F)$, $N''(\varepsilon_F)$, $N'''(\varepsilon_F)$, $N''''(\varepsilon_F)$ are the first, second, third, and fourth derivatives of the electronic density of states $N(\varepsilon_F)$ taken at the Fermi level, N_{Er} is the concentration of Er ions on which the moments of the $4f$ electrons are localized (this multiplier was omitted in [64]); $J_{Er} = \frac{15}{2}$ and $g_{Er} = \frac{6}{5}$ - are the total angular momentum for the 3^+ Er ion in the ErCo_2 compound and the Lande factor [68]. In [63] the expressions for the free energy coefficients in (7) were simplified for the case when the Fermi level coincides with a local minimum of electronic density of states, thereby justifying the consideration only the second and fourth derivatives of the electronic density of states in (6).

In Ref. [6], the $s-d$ model posits that localized moments in the Heisenberg framework yield a positive coefficient, while itinerant d -electrons can contribute a negative value. This interplay allows the emergence of a first-order magnetic phase transition. Accordingly, the criterion for a first-order phase transition is established by the negativity of the fourth-order magnetization coefficient in (6). This condition manifests as a region of negative slope in the Belov-Arrott plot, which is indicative of S-shaped behavior. As previously discussed, the Belov-Arrott plots presented in Fig. 3 indicate the presence of a first-order magnetic phase transition in the annealed ErCo_2 alloy. This observation implies that the fourth-order magnetization coefficient $B(T)$, assumes negative values in the vicinity of T_C . Additionally, the magnetization curve has an S-shaped form, i.e. a first-order metamagnetic transition occurs in the field from the para- to the ferromagnetic state if the condition is met: $\frac{3}{16} < \frac{A(T)C(T)}{B(T)^2} < \frac{9}{20}$.

The influence of vacancies on the order of phase transition was evaluated by calculating the coefficient $B(T_C)$ using (7) together with estimation of the $A(T)C(T)/B(T)^2$ ratio. This calculation was based on the computed electronic density of states for ErCo_2 , $\text{Er}_{0.97}\text{Co}_2$, and $\text{ErCo}_{1.94}$ (Fig. 6), as well as experimental data obtained from both as-cast and rapidly quenched samples (Fig. 2).

The electronic densities of states (obtained by summing the curves presented in Fig. 6) were approximated using a Gaussian function within a narrow energy range near the Fermi level ε_F . The results of this approximation are summarized in Table 2.

To compute the $B_{loc}(T)$ contribution in (7), an estimation of the molecular field coefficient is required. This coefficient was determined

Table 2

Values of the state density derivatives at the Fermi level corresponding to the graphs shown in Fig. 8.

	ErCo_2	$\text{ErCo}_{1.94}$	$\text{Er}_{0.97}\text{Co}_2$
$N(\varepsilon_F)$ [state/(eV • atom Co)]	6.04	5.73	6.61
$N'(\varepsilon_F)$ [10^1 • state/eV ² • atom Co] •	-3.38	-2.81	-6.24
$N''(\varepsilon_F)$ [10^2 • state/(eV ³ • atom Co)]	-0.73	1.88	1.05
$N'''(\varepsilon_F)$ [10^3 • state/(eV ⁴ • atom Co)]	4.35	5.72	25.40
$N''''(\varepsilon_F)$ [10^4 • state/(eV ⁵ • atom Co)]	-1.61	-18.10	-46.30

by solving the system of equations outlined in reference [69].

$$\begin{cases} E = \lambda_{Er-Er} - 2\lambda_{Er-Co} \\ \theta_R = (\lambda_{Er-Er} + \lambda_{Er-Co}) C_{Er} \end{cases} \quad (8)$$

The system of equations involves the following variable (4): E - is the combined molecular field coefficients arising from the exchange interactions both within the rare earth sublattice and between the rare earth and transition metal ions; C_{Er} - Curie constant for the rare earth atoms; χ_y - exchange-enhanced susceptibility. The values of the parameters E , C_{Er} and χ_y were determined by fitting the experimental inverse susceptibility data for both as-quenched and annealed ErCo_2 samples using the following expression $1/\chi = (T - \theta_R)/(C_{Er} - \chi_y(T - EC_{Er}))$ [69]. The values are summarized in Table 3.

The calculated values of $B(T_C)$ coefficient, $A(T)C(T)/B(T)^2$ ratio and estimation of the Stoner criterion for ErCo_2 , $\text{Er}_{0.97}\text{Co}_2$, $\text{ErCo}_{1.94}$ are presented in Table 4.

The occurrence of a first-order magnetic phase transition is only possible under certain conditions: a negative value of the coefficient $B(T_C)$ at the Curie temperature, and a specific range for the ratio of the other coefficients, namely $\frac{3}{16} < \frac{A(T)C(T)}{B(T)^2} < \frac{9}{20}$. Theoretical calculations for the nominal ErCo_2 composition, as detailed in Table 4, confirm that at least one of these criteria is met. In turn, the presence of Er vacancy enhanced a positive $B(T_C)$ coefficient together with $A(T)C(T)/B(T)^2$ ratio. This collective shift in parameters moves the system outside the conditions required for a first-order transition, thereby favoring a second-order magnetic phase transition.

As illustrated in Fig. 6, the emergence of a vacancy on an Er site results in an increase in the electronic density of states at the Fermi level. Furthermore, the Fermi level shifts from the descending region of the density of states to an ascending region. This modification is a key factor responsible for changing in the magnetic behavior.

Moreover, as demonstrated by the data presented in Table 4, the introduction of a vacancy on the Er atom ensures that the d -electron system meets the Stoner criterion for band ferromagnetism ($JN(\varepsilon_F) > 1$). This leads to the appearance of Co sublattice magnetization in weaker effective fields from the rare-earth (Re) subsystem, thereby resulting in an increase of the Curie temperature (T_C). The latter were calculated as follows:

$$T_C^2 = \frac{6k_B^2 JN(\varepsilon_F) - 1}{\pi^2} \left\{ \left(\frac{N(\varepsilon_F)}{N(\varepsilon_F)} \right)^2 - \left(\frac{N''(\varepsilon_F)}{N(\varepsilon_F)} \right) \right\}^{-1}$$

The obtained variation of the Curie temperature (see Table 4) under Er site vacancy introduction is consistent with the experimental data (see Fig. 2).

Worth noting, that in the RCO_2 series the order of the transition depends sensitively on the Co-3d DOS near ε_F , which is tuned by the lattice constant (lanthanide contraction) and by the rare-earth-Co molecular field. In the Inoue-Shimizu model, $B(T) = B_{itn} + B_{loc}$, where B_{loc} scales with the R-Co exchange and thus with the de Gennes factor $(g_J - 1)^2 J(J+1)$. Because Gd and Tb have larger de Gennes factors [70], B_{loc} is more positive and stabilizes SOPT; vacancy-induced changes in B_{itn} (via derivatives of the Co-3d DOS at ε_F) are therefore insufficient to alter the order. By contrast, Er/Ho lie closer to the critical boundary (smaller B_{loc}); the vacancy-induced increase of $N(\varepsilon_F)$ and movement of ε_F to an ascending DOS flank render $B(T_C) > 0$, i.e. SOPT, matching our

Table 3

Fitted coefficients of the inverse susceptibility for both as-cast and rapidly quenched samples, along with the corresponding molecular field coefficients derived from (4).

	θ_R , [K]	C_{Co} , [K]	χ_y	E	λ_{Er-Co}
ErCo_2	36.7	7.12		0.036	15.1
ErCo_2 melt spun	74.4	7.12		0.431	1.3

Table 4

Results of calculation of Curie temperature, Stoner's criterion $JN(\varepsilon_F)$, $A(T)C(T)/B(T)^2$ ratio and $B(T_C)$ coefficient.

	ErCo ₂	ErCo _{1.94}	Er _{0.97} Co ₂
T_C , [K]	33	74	45
$ J $, [eV]	0.180	0.162	0.203
$N(\varepsilon_F)$, [state/(eV • Co atom)]	6.038	5.730	6.610
$ J \bullet N(\varepsilon_F)$, [state/(Co atom)]	1.087	0.928	1.342
$A_{itin}(T_C)$, [(m•T)/A] • 10 ⁻⁴	4.085	3.549	14.676
$B_{itin}(T_C)$, [(m ³ •T)/A ³] • 10 ⁻¹⁶	7.713	3.342	13.807
$B_{loc}(T_C)$, [(m ³ •T)/A ³] • 10 ⁻¹⁶	0.038	0.001	0.001
$B_{total}(T_C)$, [(m•T)/A] • 10 ⁻⁴	7.751	3.343	13.808
$C_{itin}(T_C)$, [(m•T)/A] • 10 ⁻²⁸	5.841	-4.648	9.252
$A_{itin}(T_C) \bullet C_{itin}(T_C) / B_{itin}^2(T_C)$	0.401	-1.477	0.712

BA/n(T) analysis.

6. Conclusion

This study demonstrates that rapid quenching significantly alters the magnetocaloric properties of RCO_2 ($R = Er, Ho$) compounds by inducing a shift from first- to second-order magnetic phase transitions. The observed suppression of the magnetocaloric effect in as-quenched $ErCo_2$ and $HoCo_2$, accompanied by the increase in Curie temperature and spontaneous magnetization, is attributed to the formation of Er sub-lattice vacancies. Both experimental and computational analyses confirm that these vacancies modify the electronic density of states near the Fermi level, thereby enhancing the fulfillment Stoner criterion for ferromagnetism and favoring the stabilization of a second-order transition. Annealing reverses these effects, restoring the first-order transition behavior and the associated large magnetocaloric response. In contrast, RCO_2 compounds with second-order transitions ($R = Tb, Gd$) remain unaffected by rapid quenching.

This study also offers critical insights into the design of efficient heat exchangers for cryogenic magnetic refrigeration. Numerical simulations reveal that plate-type regenerators with optimized geometry outperform packed-bed configurations, particularly when gaseous helium is employed as a heat transfer medium. The enhanced cooling power of 30 μm -thick plates is attributed to their reduced porosity and improved heat transfer characteristics, which collectively enable operation at higher frequencies. Rapid quenching is identified as a viable technique for producing thin, mechanically stable ribbons with tunable magnetocaloric properties. These findings advance the development of high-performance magnetocaloric materials for next-generation cooling technologies, underscoring the critical interdependence between microstructure, electronic structure, and thermodynamic performance.

CRediT authorship contribution statement

Sviridova Tatyana: Validation, Methodology, Investigation. **Zheleznyi Mark:** Writing – review & editing, Project administration, Investigation, Funding acquisition, Formal analysis, Conceptualization. **Argunov Efim:** Conceptualization, Methodology, Resources, Software, Writing – review & editing. **Karpenkov Dmitriy:** Writing – original draft, Visualization, Supervision, Methodology, Investigation, Data curation, Conceptualization. **Tatyana B. Shapaeva:** Formal analysis, Investigation, Methodology, Writing – review & editing. **Kvashnin Alexander:** Writing – review & editing, Visualization, Validation, Software, Resources. **Karpenkov Alexey:** Methodology, Investigation. **Makarin Rodion:** Writing – original draft, Validation, Software, Methodology, Investigation, Formal analysis, Conceptualization. **Christian Tantardini:** Writing – review & editing, Visualization, Validation, Software, Resources.

Declaration of Competing Interest

The authors declare that they have no known competing financial interests or personal relationships that could have appeared to influence the work reported in this paper.

Acknowledgments

This work was supported by RSF grant 25-22-00371. RAM thanks the BASIS Foundation for scholarship support. Magnetic measurements were supported by the State Assignment for basic research under Project using equipment purchased with funds from the development program of Lomonosov Moscow State University.

References

- [1] Y. Wang, H. Pan, S. Liu, Research progress of high efficiency magnetic refrigeration technology and magnetic materials, *J. Supercond. Nov. Magn.* 38 (2025) 86, <https://doi.org/10.1007/s10948-024-06847-x>.
- [2] J.J.B. Levinsky, B. Beckmann, T. Gottschall, D. Koch, M. Ahmadi, O. Gutfleisch, G. R. Blake, Giant magnetocaloric effect in a rare-earth-free layered coordination polymer at liquid hydrogen temperatures, *Nat. Commun.* 15 (2024) 8559, <https://doi.org/10.1038/s41467-024-52879-x>.
- [3] Y. Xie, J. Wang, F. Yang, J. Ying, Y. Zhang, Magnetic phase transition and cryogenic magnetocaloric properties in the RE6Ni2.3In0.7 (RE = Ho, Er, and Tm) compounds, *J. Appl. Phys.* 136 (2024) 123910, <https://doi.org/10.1063/5.0232241>.
- [4] X. Tang, H. Sepehri-Amin, N. Terada, A. Martin-Cid, I. Kurniawan, S. Kobayashi, Y. Kotani, H. Takeya, J. Lai, Y. Matsushita, T. Ohkubo, Y. Miura, T. Nakamura, K. Hono, Magnetic refrigeration material operating at a full temperature range required for hydrogen liquefaction, *Nat. Commun.* 13 (2022) 1817, <https://doi.org/10.1038/s41467-022-29340-2>.
- [5] E. Bykov, A. Karpenkov, W. Liu, M. Straßheim, T. Niehoff, K. Skokov, F. Scheibel, O. Gutfleisch, C. Salazar Mejía, J. Wosnitza, T. Gottschall, Magnetocaloric effect in the laves phases RCO_2 ($R = Er, Ho, Dy$, and Tb) in high magnetic fields, *J. Alloy. Compd.* 977 (2024) 173289, <https://doi.org/10.1016/j.jallcom.2023.173289>.
- [6] G.A. Politova, I.S. Tereshina, A.Yu Karpenkov, V.B. Chzhan, J. Cwik, Magnetism, magnetocaloric and magnetostrictive effects in RCO_2 – type ($R = Tb, Dy, Ho$) laves phase compounds, *J. Magn. Magn. Mater.* 591 (2024) 171700, <https://doi.org/10.1016/j.jmmm.2023.171700>.
- [7] J. Herrero-Albillos, F. Bartolomé, L.M. García, F. Casanova, A. Labarta, X. Batlle, Nature and entropy content of the ordering transitions in Co_2 , *Phys. Rev. B* 73 (2006) 134410, <https://doi.org/10.1103/PhysRevB.73.134410>.
- [8] N.K. Singh, K.G. Suresh, A.K. Nigam, S.K. Malik, A.A. Coelho, S. Gama, Itinerant electron metamagnetism and magnetocaloric effect in RCO_2 -based laves phase compounds, *J. Magn. Magn. Mater.* 317 (2007) 68–79, <https://doi.org/10.1016/j.jmmm.2007.04.009>.
- [9] J.Y. Law, V. Franco, L.M. Moreno-Ramírez, A. Conde, D.Y. Karpenkov, I. Radulov, K.P. Skokov, O. Gutfleisch, A quantitative criterion for determining the order of magnetic phase transitions using the magnetocaloric effect, *Nat. Commun.* 9 (2018) 2680, <https://doi.org/10.1038/s41467-018-05111-w>.
- [10] K. Morrison, A. Dupas, Y. Mudryk, V.K. Pecharsky, K.A. Gschneidner, A.D. Caplin, L.F. Cohen, Identifying the critical point of the weakly first-order itinerant magnet $DyCoS$ with complementary magnetization and calorimetric measurements, *Phys. Rev. B* 87 (2013) 134421, <https://doi.org/10.1103/PhysRevB.87.134421>.
- [11] N.A. Zarkevich, V.I. Zverev, Viable materials with a giant magnetocaloric effect, *Crystals* 10 (2020), <https://doi.org/10.3390/crys10090815>.
- [12] O. Syschenko, V. Sechovský, M. Diviš, T. Fujita, R. Hauser, H. Fujii, Magnetism in rare earth Co_2 compounds under high pressures, *J. Appl. Phys.* 89 (2001) 7323–7325, <https://doi.org/10.1063/1.1359459>.
- [13] N. Ishimatsu, S. Miyamoto, H. Maruyama, J. Chaboy, M.A. Laguna-Marco, N. Kawamura, Experimental evidence of pressure-induced suppression of the cobalt magnetic moment in $ErCo_2$, *Phys. Rev. B* 75 (2007) 180402, <https://doi.org/10.1103/PhysRevB.75.180402>.
- [14] Z. Śniadecki, N. Pierunek, B. Idzikowski, B. Wasilewski, M. Werwiński, U.K. Rößler, Yu Ivanisenko, Influence of structural disorder on the magnetic properties and electronic structure of YCo_2 , *Phys. Rev. B* 98 (2018) 094418, <https://doi.org/10.1103/PhysRevB.98.094418>.
- [15] T.D. Yamamoto, A.T. Saito, H. Takeya, K. Terashima, T. Numazawa, Y. Takano, Tunable magnetic and magnetocaloric properties by thermal annealing in $ErCo_2$ atomized particles, *J. Alloy. Compd.* 935 (2023) 168040, <https://doi.org/10.1016/j.jallcom.2022.168040>.
- [16] S.D. Das, N. Mohapatra, K.K. Iyer, R.D. Bapat, E.V. Sampathkumaran, Magnetic behavior of nanocrystalline $ErCo_2$, *J. Phys. Condens. Matter* 21 (2009) 296004, <https://doi.org/10.1088/0953-8984/21/29/296004>.
- [17] N.H. Duc, T.D. Hien, P.E. Brommer, J.J.M. Franse, Magnetic properties of the Er (Co_1-xCu_x)₂ and Y (Co_1-xCu_x)₂ compounds, *Phys. B+C* 149 (1988) 352–360, [https://doi.org/10.1016/0378-4363\(88\)90266-5](https://doi.org/10.1016/0378-4363(88)90266-5).
- [18] M.R. Soares, A.Y. Takeuchi, F. Garcia, S.F. da Cunha, M. El Massalami, Magnetic phase diagram of the intermetallic series Er (Co_1-xNix)₂, *J. Magn. Magn. Mater.* 202 (1999) 473–479, [https://doi.org/10.1016/S0304-8853\(99\)00394-7](https://doi.org/10.1016/S0304-8853(99)00394-7).

- [19] S. Daniš, P. Javorský, D. Rafaja, V. Sechovský, Low-temperature transport and crystallographic studies of Er(Co_{1-x}Six)2 and Er(Co_{1-x}Gex)2, *J. Alloy. Compd.* 345 (2002) 54–58, [https://doi.org/10.1016/S0925-8388\(02\)00397-3](https://doi.org/10.1016/S0925-8388(02)00397-3).
- [20] J. Prokleska, J. Vejpravová, D. Vasylev, V. Sechovský, Magnetism of Er(Co_{1-x}Xx)2 compounds: effects on structure and electronic properties, *J. Alloy. Compd.* 383 (2004) 122–125, <https://doi.org/10.1016/j.jallcom.2004.04.020>.
- [21] X.B. Liu, Z. Altounian, Magnetocaloric effect in Co-rich Er(Co_{1-x}Fex)2 laves phase, *J. Appl. Phys.* 103 (2008) 07B304, <https://doi.org/10.1063/1.2829758>.
- [22] J.-D. Zou, M. Yan, J.-L. Yao, Manipulation of the magnetic properties in Er_{1-x}Co_x compounds by atomic vacancies, *J. Alloy. Compd.* 632 (2015) 30–36, <https://doi.org/10.1016/j.jallcom.2015.01.122>.
- [23] M. Cyrot, D. Gignoux, F. Givord, M. Lavagna, Magnetism of the rare earth, 3d – theoretical review, *J. De. Phys. Colloq.* 40 (C5) (1979) 171–C5-176, <https://doi.org/10.1051/jphscol:1979563>.
- [24] A.T. Burkov, E. Bauer, E. Gratz, R. Resel, T. Nakama, K. Yagasaki, Effect of static and dynamic disorder on electronic transport in RC₂O compounds: Ho(AlxCo_{1-x})₂ alloys, *Phys. Rev. B* 78 (2008) 035101, <https://doi.org/10.1103/PhysRevB.78.035101>.
- [25] V.V. Aleksandryan, K.P. Belov, R.Z. Levitin, A.S. Markosyan, V.V. Snegirev, Giant increase in the curie temperature of RC₂O intermetallic rare-earth compounds at low degrees of replacement of magnetic cobalt by nonmagnetic aluminum, *JETP Lett.* 40 (1984) 77. (http://jetpletters.ru/ps/0/article_18963.shtml).
- [26] D.Y. Karpenkov, K.P. Skokov, J. Liu, A.Y. Karpenkov, E.M. Semenova, E.L. Airiyani, Y.G. Pastushenkov, O. Gutefleisch, Adiabatic temperature change of micro- and nanocrystalline Y₂Fe₁₇ heat-exchangers for magnetic cooling, *J. Alloy. Compd.* 668 (2016) 40–45, <https://doi.org/10.1016/j.jallcom.2016.01.209>.
- [27] D.Yu Karpenkov, R.A. Makarin, A.Yu Karpenkov, A.V. Korotitskiy, A.S. Komlev, M. V. Zheleznyi, Adjusting of the performance characteristics of the La(Fe,Si)₁₃ compounds and their hydrides for multi-stimuli cooling cycle application, *J. Alloy. Compd.* 962 (2023) 171154, <https://doi.org/10.1016/j.jallcom.2023.171154>.
- [28] A.I. Liechtenstein, V.I. Anisimov, J. Zaanen, Density-functional theory and strong interactions: orbital ordering in Mott-Hubbard insulators, *Phys. Rev. B* 52 (1995) R5467–R5470, <https://doi.org/10.1103/PhysRevB.52.R5467>.
- [29] J.P. Perdew, K. Burke, M. Ernzerhof, Generalized gradient approximation made simple, *Phys. Rev. Lett.* 77 (1996) 3865–3868, <https://doi.org/10.1103/PhysRevLett.77.3865>.
- [30] D.R. Hamann, Optimized norm-conserving vanderbilt pseudopotentials, *Phys. Rev. B* 88 (2013) 085117, <https://doi.org/10.1103/PhysRevB.88.085117>.
- [31] M.J. van Setten, M. Giantomassi, E. Bousquet, M.J. Verstraete, D.R. Hamann, X. Gonze, G.-M. Rignanese, The PseudoDojo: training and grading a 85 element optimized norm-conserving pseudopotential table, *Comput. Phys. Commun.* 226 (2018) 39–54, <https://doi.org/10.1016/j.cpc.2018.01.012>.
- [32] E.A. Quadrelli, Lanthanide contraction over the 4f series follows a quadratic decay, *Inorg. Chem.* 41 (2002) 167–169, <https://doi.org/10.1021/ic015580v>.
- [33] C.G. BROYDEN, The convergence of a class of Double-rank minimization algorithms 1. General considerations, *IMA J. Appl. Math.* 6 (1970) 76–90, <https://doi.org/10.1093/imamat/6.1.76>.
- [34] D. Goldfarb, A family of Variable-Metric methods derived by variational means, *Math. Comput.* 24 (1970) 23–26, <https://doi.org/10.2307/2004873>.
- [35] D.F. Shanno, Conditioning of Quasi-Newton methods for function minimization, *Math. Comput.* 24 (1970) 647–656, <https://doi.org/10.2307/2004840>.
- [36] Fletcher, R. Ch. Grossmann, Unconstrained optimization. Practical methods of optimization 1. Chichester-new York-Brisbane-Toronto, John Wiley&Sons 1980. Viii, 408-408, 120 S. £ 8. 80. ISBN 0471277118 ZAMM J. Appl. Math. Mech. / Z. Für. Angew. Math. Mech. 61 (1981), <https://doi.org/10.1002/zamm.19810610824>.
- [37] D.P. Kozlenko, E. Burzo, P. Vlaic, S.E. Kichanov, A.V. Rutkauskas, B.N. Savenko, Sequential cobalt magnetization collapse in ErCo₂: beyond the limits of itinerant electron metamagnetism, *Sci. Rep.* 5 (2015) 8620, <https://doi.org/10.1038/srep08620>.
- [38] J. Herrero-Albillos, F. Bartolomé, L.M. García, A.T. Young, T. Funk, J. Campo, G. J. Cuello, Observation of a different magnetic disorder in ErCo₂, *Phys. Rev. B* 76 (2007) 094409, <https://doi.org/10.1103/PhysRevB.76.094409>.
- [39] P. Giannozzi, S. Baroni, N. Bonini, M. Calandra, R. Car, C. Cavazzoni, D. Ceresoli, G.L. Chiarotti, M. Cococcioni, I. Dabo, A. Dal Corso, S. de Gironcoli, S. Fabris, G. Fratesi, R. Gebauer, U. Gerstmann, C. Gougaud, A. Kokalj, M. Lazzeri, L. Martin-Samos, N. Marzari, F. Mauri, R. Mazzarello, S. Paolini, A. Pasquarello, L. Paulatto, C. Sbraccia, S. Scandolo, G. Scalauzero, A.P. Seitsonen, A. Smogunov, P. Umari, R.M. Wentzcovitch, QUANTUM ESPRESSO: a modular and open-source software project for quantum simulations of materials, *J. Phys. Condens. Matter* 21 (2009) 395502, <https://doi.org/10.1088/0953-8984/21/39/395502>.
- [40] P. Giannozzi, O. Andreussi, T. Brumme, O. Bunau, M. Buongiorno Nardelli, M. Calandra, R. Car, C. Cavazzoni, D. Ceresoli, M. Cococcioni, N. Colonna, I. Carnimeo, A. Dal Corso, S. de Gironcoli, P. Delugas, R.A. DiStasio, A. Ferretti, A. Floris, G. Fratesi, G. Fugallo, R. Gebauer, U. Gerstmann, F. Giustino, T. Gorni, J. Jia, M. Kawamura, H.-Y. Ko, A. Kokalj, E. Küçükberenli, M. Lazzeri, M. Marsili, N. Marzari, F. Mauri, N.L. Nguyen, H.-V. Nguyen, A. Otero-de-la-Roza, L. Paulatto, S. Poncè, D. Rocca, R. Sabatini, B. Santra, M. Schlipf, A.P. Seitsonen, A. Smogunov, I. Timrov, T. Thonhauser, P. Umari, N. Vast, X. Wu, S. Baroni, Advanced capabilities for materials modelling with quantum ESPRESSO, *J. Phys. Condens. Matter* 29 (2017) 465901, <https://doi.org/10.1088/1361-648X/aa8f79>.
- [41] W. Kohn, N. Rostoker, Solution of the schrödinger equation in periodic lattices with an application to metallic lithium, *Phys. Rev.* 94 (1954) 1111–1120, <https://doi.org/10.1103/PhysRev.94.1111>.
- [42] K.H. Johnson, “Multiple-Scattering” model for polyatomic molecules, *J. Chem. Phys.* 45 (1966) 3085–3095, <https://doi.org/10.1063/1.1728065>.
- [43] F. Herman, A.R. Williams, K.H. Johnson, Multiple scattering method based on overlapping atomic spheres with application to the TCNQ molecule, *J. Chem. Phys.* 61 (1974) 3508–3522, <https://doi.org/10.1063/1.1682531>.
- [44] H. Akai, P.H. Dederichs, Local moment disorder in ferromagnetic alloys, *Phys. Rev. B* 47 (1993) 8739–8747, <https://doi.org/10.1103/PhysRevB.47.8739>.
- [45] H. Akai, Fast Korringa-Kohn-Rostoker coherent potential approximation and its application to FCC Ni-Fe systems, *J. Phys. Condens. Matter* 1 (1989) 8045, <https://doi.org/10.1088/0953-8984/1/43/006>.
- [46] H. Akai, AkaiKKR (Machikaneyama), (n.d.). (<http://kkr.issp.u-tokyo.ac.jp>).
- [47] K. Koepenik, B. Velický, R. Hayn, H. Eschrig, Self-consistent LCAO-CPA method for disordered alloys, *Phys. Rev. B* 55 (1997) 5717–5729, <https://doi.org/10.1103/PhysRevB.55.5717>.
- [48] G.M. Stocks, W.M. Temmerman, B.L. Gyorffy, Complete solution of the Korringa-Kohn-Rostoker Coherent-Potential-Approximation equations: Cu-Ni alloys, *Phys. Rev. Lett.* 41 (1978) 339–343, <https://doi.org/10.1103/PhysRevLett.41.339>.
- [49] D.A. Nield, A. Bejan, Convection in porous media, Springer International Publishing, Cham, 2017, <https://doi.org/10.1007/978-3-319-49562-0>.
- [50] A.P. de Wasch, G.F. Froment, A two dimensional heterogeneous model for fixed bed catalytic reactors, *Chem. Eng. Sci.* 26 (1971) 629–634, [https://doi.org/10.1016/0009-2509\(71\)86006-2](https://doi.org/10.1016/0009-2509(71)86006-2).
- [51] D. Li, Y. Homma, F. Honda, T. Yamamura, D. Aoki, Large magnetocaloric effect and magnetic properties in ErCoAl, *Phys. Procedia* 75 (2015) 1300–1305, <https://doi.org/10.1016/j.phpro.2015.12.145>.
- [52] K. Dadda, S. Alleg, J. Saurina, L. Escoda, J.-J. Suñol, Structure, microstructure, and magnetic properties of melt spun Ni50Mn50–xInx ribbons, *Magnetochemistry* 7 (2021), <https://doi.org/10.3390/magnetochemistry7050063>.
- [53] A.V. Arkhipov, S.V. Andreev, D.S. Neznakhin, A.V. Tebenkov, A. Larrañaga, G. V. Kurlyandskaya, A.V. Svalov, Role of mechanical treatments in the formation of magnetocaloric properties of gd melt spun ribbons, *AIP Conf. Proc.* 2313 (2020) 030036, <https://doi.org/10.1063/5.0032547>.
- [54] A.S. Kumar, M.V. Ramudu, Seshubai, The role of quenched-in disorder in polycrystalline bulk and melt-spun ribbons of Ni50Mn29Ga21, *Phase Transit.* 94 (2021) 183–191, <https://doi.org/10.1080/01411594.2021.1928125>.
- [55] T. Haraguchi, K. Yoshimi, H. Kato, S. Hanada, A. Inoue, Determination of density and vacancy concentration in rapidly solidified FeAl ribbons, *Intermetallics* 11 (2003) 707–711, [https://doi.org/10.1016/S0966-9795\(03\)00066-9](https://doi.org/10.1016/S0966-9795(03)00066-9).
- [56] M. Yamaguchi, Y. Shirai, Defect structures, in: N.S. Stoloff, V.K. Sikka (Eds.), *Physical Metallurgy and Processing of Intermetallic Compounds*, Springer US, Boston, MA, 1996, pp. 3–27, https://doi.org/10.1007/978-1-4613-1215-4_1.
- [57] Y. Kraftmakher, Equilibrium vacancies and thermophysical properties of metals, *Phys. Rep.* 299 (1998) 79–188, [https://doi.org/10.1016/S0370-1573\(97\)00082-3](https://doi.org/10.1016/S0370-1573(97)00082-3).
- [58] I. Serhiienko, M. Parzer, F. Garmroudi, A. Novitskii, N.Tsujii Tarachand, E. Bauer, Y. Grin, T. Mori, Pivotal role of sb vacancies in quaternary half-Heusler thermoelectrics, *J. Mater. Chem. A* (2025), <https://doi.org/10.1039/DSTA01437A>.
- [59] E. Schafler, G. Steiner, E. Korznikova, M. Kerber, M.J. Zehtbauer, Lattice defect investigation of ECAP-Cu by means of X-ray line profile analysis, calorimetry and electrical resistometry, *Mater. Sci. Eng. A* 410411 (2005) 169–173, <https://doi.org/10.1016/j.msea.2005.08.070>.
- [60] D.M. Edwards, E.P. Wohlfarth, H. Jones, Magnetic isotherms in the band model of ferromagnetism, *Proc. R. Soc. Lond. Ser. A. Math. Phys. Sci.* 303 (1968) 127–137, <https://doi.org/10.1098/rspa.1968.0043>.
- [61] E.P. Wohlfarth, P. Rhodes, Collective electron metamagnetism, *Philos. Mag. A J. Theor. Exp. Appl. Phys.* 7 (1962) 1817–1824, <https://doi.org/10.1080/1478436208213848>.
- [62] N.H. Duc, P.E. Brommer, Chapter 3 formation of 3d-moments and spin fluctuations in some rare-earth-cobalt compounds, in: *Handbook of Magnetic Materials*, Elsevier, 1999, pp. 259–394, [https://doi.org/10.1016/S1567-2719\(99\)12007-9](https://doi.org/10.1016/S1567-2719(99)12007-9).
- [63] D. Bloch, D.M. Edwards, M. Shimizu, J. Voiron, First order transitions in AC₂ compounds, *J. Phys. F Met. Phys.* 5 (1975) 1217, <https://doi.org/10.1088/0305-4608/5/6/022>.
- [64] R.Z. Levitin, A.S. Markosyan, Itinerant metamagnetism, *Sov. Phys. Usp.* 31 (1988) 730, <https://doi.org/10.1070/PU1988v03n08ABEH004922>.
- [65] J. Inoue, M. Shimizu, Volume dependence of the first-order transition temperature for RC₂ compounds, *J. Phys. F Met. Phys.* 12 (1982) 1811, <https://doi.org/10.1088/0305-4608/12/8/021>.
- [66] J. Inoue, M. Shimizu, First- and second-order magnetic phase transitions in (R-Y) Co₂ and R(Co-Al)2 (R=heavy rare-earth element) compounds, *J. Phys. F Met. Phys.* 18 (1988) 2487, <https://doi.org/10.1088/0305-4608/18/11/020>.
- [67] V. Heine, s'ensuremagnet-d interaction in transition metals, *Phys. Rev.* 153 (1967) 673–682, <https://doi.org/10.1103/PhysRev.153.673>.
- [68] R.J. Radwański, The intersublattice molecular fields in the rare earth–cobalt intermetallics, *Phys. Status Solidi (b)* 137 (1986) 487–493, <https://doi.org/10.1002/pssb.2221370210>.
- [69] D. Bloch, R. Lemaire, Metallic alloys and exchange-enhanced paramagnetism. application to rare-earth–cobalt alloys, *Phys. Rev. B* (1970) 2648–2650, <https://doi.org/10.1103/PhysRevB.2.2648>.
- [70] E. Burzo, P. Vlaic, D.P. Kozlenko, A.V. Rutkauskas, High-pressure neutron diffraction study of RC₂ compounds, *J. Phys. Chem. Solids* 160 (2022) 110330, <https://doi.org/10.1016/j.jpcs.2021.110330>.